Comparison of two depth averaged numerical models for debris flow runout estimation

Vagnon Federico*

Department of Earth Science, University of Torino, Via Valperga Caluso 35, 10125, Turin, Italy.

*Corresponding author: fvagnon@unito.it, Tel: +39 0116705325

Pirulli Marina

Department of Structural, Geotechnical and Building Engineering, Politecnico di Torino, Corso Duca degli Abruzzi 24, 10129 Turin, Italy

marina.pirulli@polito.it

Yague Angel

Department of Applied Mathematics and Computer Science, ETSI Caminos, Canales y Puertos, Universidad Politécnica de Madrid (UPM), Madrid, Spain

angel.yague@upm.es

Pastor Manuel

Department of Applied Mathematics and Computer Science, ETSI Caminos, Canales y Puertos, Universidad Politécnica de Madrid (UPM), Madrid, Spain

manuel.pastor@upm.es

Abstract

This paper analyses an important aspect of the continuum numerical modeling of rapid landslides as debris flows: by using the same rheological parameter values, are the results, obtained with codes that implement the same constitutive equations but a different numerical solver, equal? In order to answer this question, the two numerical codes RASH3D and GeoFlow_SPH are here used to back-analyze the debris flow event occurred in the Nora stream (Northwestern Italian Alps) in October 2000. Comparison of results evidenced that the RASH3D best fit rheological values for the Nora event back analysis overestimated both the final depositional heights and the simulated flow velocities if used in GeoFlow_SPH. In order to obtain thickness values comparable with those measured in situ, it was necessary to re-calibrate GeoFlow_SPH rheological parameter values. In this way, with the exception of a larger lateral spreading of the sliding mass given by RASH3D, both thickness and velocity values were similar for the two numerical codes.

Keywords

Debris flow; runout estimation; RASH3D code; GeoFlow_SPH code; continuum numerical modelling

40 # 1. Introduction

41 Every year thousands of landslides all over the world cause loss of human lives and
42 enormous economical damages. These phenomena remember us of our society's
43 vulnerability to natural disasters (Jakob and Hungr 2005).

44 In the last decades, the climate changes have increased the probability of occurrence of a
45 particular type of landslide: the debris flow. Glacier melting, permafrost degradation,
46 increase of extreme (short and intense) rainfall are triggering factors for this dangerous
47 and destructive phenomenon. The main characteristics of debris flows are their
48 unpredictability, their high velocity and their long travel distances.

49 Since their potential for destruction usually cannot practically be reduced by stabilization
50 of the source area (Hungr 1995), engineering risk analyses are required, including
51 prediction of runout parameters (maximum travel distance reached, flow velocities,
52 thickness and distribution of the deposit). Since it is very difficult to obtain data from
53 monitoring of real events and to apply statistical methods, others methodologies for
54 evaluating flow characteristics are required. Numerical models represent a useful tool for
55 investigating, within realistic geological contexts, the dynamics of these events.

56 Existing models can be divided into two main groups: those that follow empirical
57 approaches and those that are based on dynamic numerical models (continuum or
58 discontinuum). Empirical models, based on correlation among historical data (e.g. Cannon
59 1993, Corominas 1996, Rickenmann 1999), are more practical and easy to use but they
60 should only be applied to conditions similar to those on which their development are based
61 (Rickenmann 2005).

62 Alternatively, dynamic numerical models are viable tools for forecasting flow parameters
63 (e.g. Savage and Hutter 1989, O'Brien et al. 1993, Hungr 1995, Iverson and Delinger
64 2001, Mc-Dougall and Hungr 2004, Pirulli 2005, Pastor et al. 2009). In particular, the
65 basic concept of continuum-based methods is that the release mass dynamics can be

66 described in terms of flow-like behaviour. The moving mass can entrain additional
67 material from the path and eventually deposits, when it reaches slopes that are sufficiently
68 flat. Whatever code is used, the choice of the rheological law, the terrain characteristics
69 and the presence of erosion/deposition areas affect the results (Pirulli and Marco, 2010).
70 Consequently, these methods require an accurate calibration of parameters on the basis of
71 back analysis of real events for assessing and forecasting potential dangerous areas.
72 Another important issue is the choice of the most suitable simulation code: Pirulli and
73 Sorbino (2008) stated that the use of more than one code for simulating debris flow events
74 is recommended in order to compare runout results, providing and highlighting the main
75 differences. This aspect is particularly important because it helps users in the decisional
76 process for assessing potential risks and evaluating/designing possible countermeasures.
77 The purpose of this paper is to investigate if codes that implement the same governing
78 equations, but with fundamentally different numerical solvers, produce different results,
79 when the same rheological law and rheological values are used to model a given case, and
80 the extent to which obtained results may differ. This is an important aspect and it should
81 be taken into account by the engineers (e.g. in the design of structural countermeasures
82 and mapping of dangerous areas). Since one of the main functions of the numerical codes
83 should be to forecast future events and to predict their effects, their choice becomes, for
84 the engineers, an important aspect to take into account (Vagnon 2017).
85 In the following sections the two different continuum-based codes RASH3D (Pirulli 2005)
86 and GeoFlow_SPH (Pastor et al. 2009, 2015) are briefly described and used to back-
87 analyze a real debris flow event occurred in Northern Italy. The obtained results are
88 compared and discussed.
89

2. Continuum mechanics modeling

To apply continuum mechanics to flow-like landslide modeling implies that both characteristic thickness (H) and length (L) of the flowing mass are assumed to exceed the size of single moving particles of several times. With this hypothesis, the real moving mixture, composed of solid and fluid phases, can be replaced by an "equivalent fluid", whose properties have to approximate the bulk behaviour of the real mixture.

Furthermore, a kinematic boundary condition is imposed on free and bed surfaces according to which the mass neither enters nor leaves at these two surfaces unless an erosion law is introduced.

Under the above conditions and assuming that the sliding mass is described as a single-phase, incompressible and homogeneous material (Savage and Hutter 1989, Hungr 1995, Iverson and Delinger 2001), the motion can be described using the balance of mass and momentum equations:

$$\nabla \cdot v = 0 \tag{1}$$

$$\rho\left(\frac{\partial v}{\partial t} + v \cdot \nabla v\right) = -\nabla \cdot \sigma + \rho g \tag{2}$$

where $v = (v_x, v_y, v_z)$ denotes the three-dimensional velocity vector inside the mass in a (x, y, z) coordinate system that will be discussed later, $\sigma(x, y, z, t)$ is the Cauchy stress tensor, ρ is the mass density and g is the vector of gravitational acceleration.

Depth averaging of these equations and shallow flow assumption require the choice of an appropriate coordinate system. During the flow, the characteristic thickness (H) of the flow is considerably smaller than its extent parallel to the bed (L). In the case of significant slopes, the shallow flow assumption is more significant in a reference frame linked to the topography and the classical shallow water approximation relating horizontal and vertical direction is not appropriate (Mangeney-Castelnau et al. 2003). As in the work by Denlinger and Iverson (2001), the equations are here written in term of a local,

orthogonal Cartesian coordinate system in which the z coordinate is normal to the local topography.

In the reference frame linked to the topography, equations of mass and momentum in the x and y direction derived by integration of Navier-Stokes equations (1)-(2) read

$$\begin{cases} \dfrac{\partial h}{\partial t} + \dfrac{\partial(\overline{v_x}h)}{\partial x} + \dfrac{\partial(\overline{v_y}h)}{\partial y} = 0 \\ \rho\left(\dfrac{\partial(\overline{v_x}h)}{\partial t} + \dfrac{\partial\left(\overline{v_x^2}h\right)}{\partial x} + \dfrac{\partial(\overline{v_x v_y}h)}{\partial y}\right) = \mp\dfrac{\partial(\overline{\sigma_{xx}}h)}{\partial x} + \dfrac{\partial(\overline{\sigma_{xy}}h)}{\partial y} + T_{x_{(z=b)}} + \rho g_x h \\ \rho\left(\dfrac{\partial(\overline{v_y}h)}{\partial t} + \dfrac{\partial(\overline{v_y v_x}h)}{\partial x} + \dfrac{\partial\left(\overline{v_y^2}h\right)}{\partial y}\right) = +\dfrac{\partial(\overline{\sigma_{xy}}h)}{\partial x} \mp \dfrac{\partial(\overline{\sigma_{yy}}h)}{\partial y} + T_{y_{(z=b)}} + \rho g_y h \end{cases} \quad (3)$$

where $\bar{v} = (\overline{v_x}, \overline{v_y})$ denotes the depth-averaged flow velocity, h is the flow depth, T_x and T_y are the traction vector components in the x and y directions and g_x, g_y are the projections of the gravity vector along the x and y directions, respectively. The traction vector T = (Tx, Ty, Tz) = - $\sigma \cdot n_b$, where n_b is the unit vector normal to the bed, read

$$T = \begin{pmatrix} \sigma_{xx}\dfrac{\partial b}{\partial x} + \sigma_{xy}\dfrac{\partial b}{\partial y} - \sigma_{xz} \\ \sigma_{xy}\dfrac{\partial b}{\partial x} + \sigma_{yy}\dfrac{\partial b}{\partial y} - \sigma_{yz} \\ \sigma_{xz}\dfrac{\partial b}{\partial x} + \sigma_{yz}\dfrac{\partial b}{\partial y} - \sigma_{zz} \end{pmatrix}_b$$

A scale analysis with respect to H/L (Gray et al. 1999, Mangeney-Castelnau et al. 2003) leads to neglect the acceleration normal to the topography and the horizontal gradients of the stresses in the z equation, leading to $\sigma_{zz} = \rho g_z(h-z)$. The normal traction reduced to Tz = - $\sigma_{zz|b}$ and $(\partial/\partial x_i)\left(h\bar{\sigma}_{xy}\right)$ can be neglected in the z and y depth-averaged momentum equations.

Depth-average integration simplifies the three-dimensional description of the flow but the vertical velocity distribution is lost and replaced with a single average velocity value in the flow depth for each point of the flowing mass. Furthermore, the rheological characteristics are included in a single term acting at the interface between flow and terrain surface.

In 1989 depth-averaged equations were applied for the first time to the analysis of propagation of a granular mass by Savage and Hutter; since then, many numerical models were progressively implemented. Even if based on the same balance equations and the same simplifying hypotheses, the above codes mainly differ for the adopted numerical solver.

In the following sections, the characteristics and peculiarity of the two continuum numerical codes, RASH3D (Pirulli 2005) and GeoFlow_SPH (Pastor et al. 2009, 2015), are presented, focusing on both similarities and main differences.

3. RASH3D versus GeoFlow_SPH

In continuum dynamics, the equations of motion can be formulated in one of two frames of reference: Eulerian or Langrangian. A Eulerian reference frame is fixed in space, while a Lagrangian reference frame moves with the flow. Furthermore, to perform the mass balance calculation, a discretisation of the equations has to be made by using a mesh (structured or unstructured) or a meshless approach. In a meshless scheme, in lieu of a mesh, balance is determined from the spatial distribution of a number of moving reference masses (known as particles). The RASH3D and GeoFlow_SPH codes adopt the first and the second discretization-approach, respectively. In particular, RASH3D discretizes the terrain on a general triangular grid with a finite element data structure and it computes the flow in the different flow directions using a particular control volume; whereas, in GeoFlow_SPH, the sliding soil is schematized as a series of nodes with fictitious moving mass and pressure terms. That is, RASH3D uses a Eulerian method and a fixed reference system for evaluating flow motion characteristics (for each node of the mesh, velocity and thickness and their evolution in time are calculated). On the other hand, GeoFlow_SPH uses a meshless Langrangian method known as Smoothed Particle Hydrodynamics (SPH) and the reference system is integral with the particle position.

160 Both these codes are based on a depth-average continuum mechanics based approach and
161 they need as input data to run an analysis: i) the pre-event digital elevation model (DEM),
162 ii) the position and the magnitude of a source area, iii) the rheological law.
163 A relation deduced from the mechanical behaviour of the material has to be imposed
164 between the tangential stress $T_t = (T_x, T_y)$ and v and h in order to close equations (3). The
165 depth-averaged mass is then considered as an effective material submitted to an empirical
166 friction introduced in the tangential traction term T_t (Pouliquen 1999).
167 Considering a Coulomb-type friction law, the norm of the tangential traction $\|T_t\|$ at the
168 bed is related to the norm of the normal traction $\|T_n\| = |T_z| = |\sigma_{zz|b}|$ at the bed, through a
169 friction coefficient μ, that is $\|T_t\| \leq \sigma_c = \mu\|T_n\| = \mu\rho g_z h$ and acting opposite to the
170 velocity (i.e. $T_i = -\mu\rho g_z h \frac{\bar{v}_i}{\|\bar{v}\|}$). The value of σ_c defines the upper bound of the admissible
171 stresses.
172 Similarly, the Voellmy rheology gives:
173 $$T_i = -\left(\rho g_z h\mu + \frac{\rho g \bar{v}_i^2}{\xi}\right)\frac{\bar{v}_i}{\|\bar{v}\|} \quad i = (x, y) \tag{4}$$
174 where μ is the frictional coefficient equals to the tangent of the bulk basal friction angle
175 and ξ is the turbulent coefficient.
176 The Voellmy rheology, as stated by many Authors (e.g. Hungr and Evans 1996,
177 Rickenmann and Koch 1997, Revellino et al. 2004, Pirulli 2009), produces most consistent
178 results in terms of debris spreading and distribution as well as velocity data when debris
179 flows are analysed. This is why it has been selected for comparing the two codes results in
180 the case of Rio Nora debris flow event.
181 It is finally underlined that the two selected codes have been widely validated through the
182 back analysis of laboratory experiments (e.g. Manzella et al. 2008, Pisani et al. 2013,
183 Sauthier et al. 2015) and of real events (e.g. Pirulli 2009, Pirulli and Marco 2010, Pirulli
184 and Pastor 2012, Cascini et al. 2014, Cuomo et al. 2014, Pastor et al. 2014, Pirulli 2016,

185 Dutto et al. 2017, Pirulli et al. 2017), and in the frame of a common benchmark exercise
186 (see Pastor et al. 2007, Pirulli and Scavia 2007).
187
188 **3.1. The RASH3D code**
189 The RASH3D code, developed by Pirulli (2005) is an upgrade for modelling landslide run
190 out problems of a pre-existing numerical code (SHWCIN) developed by Audusse et al.
191 (2000) using a finite volume method.
192 This type of method requires the formulation of the equations in terms of conservation
193 laws.
194 The system of equations (3), approximated in accordance with the scale analysis described
195 in "Continuum mechanics modelling" section, can be written as

196 $$\frac{\partial U}{\partial t} + divF(U) = B(U) \quad (5)$$

197 with U= $\begin{pmatrix} h \\ hv_x \\ hv_y \end{pmatrix}$, $F(U) = \begin{pmatrix} hv_x & hv_y \\ hv_x^2 + \frac{g_z h^2}{2} & hv_x v_y \\ hv_x v_y & hv_y^2 + \frac{g_z h^2}{2} \end{pmatrix}$ and $B(U) = \begin{pmatrix} 0 \\ g_x h + \frac{1}{\rho} T_x \\ g_y h + \frac{1}{\rho} T_y \end{pmatrix}$

198 The system of equations is then discretized on an unstructured triangular mesh with a
199 finite element data structure using a particular control volume, which is the median dual
200 cell (Pirulli 2005). Dual cells C_i are obtained by joining the centres of mass of the
201 triangles surrounding each vertex P_i of the mesh (Figure 1).
202 For each point P_i of the mesh the code gives as output the values in time of flow height,
203 velocity in x and y directions and the maximum values of height and velocity reached
204 during whole process up to final deposition of the mass.
205
206 **Figure 1.** Triangular finite-element mesh for dual cell C_i (adapted from Mangeney-
207 Castelnau et al. 2003). n_{ij} normal vector to Γ_{ij} directed from P_i to P_j, one of the mesh
208 vertexes that surround P_i, Γ_{ij}, boundary of the dual cell C_i separating P_i from P_j.

Under these hypotheses, the finite volume scheme writes as:

$$U_i^{n+1} = U_i^n - \sum_{j \in K_i} \frac{\Delta t L_{ij}}{|C_i|} F\left(U_i^n, U_j^n, n_{ij}\right) + \Delta t B(U_i^n) \qquad (6)$$

where U_i^{n+1}, U_i^n is the approximation of the cell average of the exact solution U for the ith cell, at times t^n and t^{n+1}, respectively, and K_i is the set of nodes P_j surrounding P_i. $F(U_i^n, U_j^n, n_{ij})$ denotes an interpolation of the normal component of the flux $F(U)\cdot n_{ij}$ along boundary edge Γ_{ij}, with length L_{ij}, which separates cells C_i and C_j (Figure 1), Δt is the time step, $|C_i|$ is the area of C_i, $B(U_i^n)$ is the approximation of the ith cell average of the exact source term, B(U), at time t^n (Audusse et al. 2000). The summation sign in the second term of the right hand side of equation (6) indicates that the computation here includes all the boundary edges of the considered ith cell. In RASH3D, a proper calculation of the projection of the term of gravity in equations (3) is obtained, for a finite volume method and a complex topography, by computing the line of maximum dip of each cell, projecting it on the plane tangent to the topography and re-projecting the obtained direction on the x and y axes of the reference system (Pirulli, 2005).

3.2. The GeoFlow_SPH model

The GeoFlow_SPH model proposed by Pastor et al. (2009) is based on the theoretical framework of Hutchinson (1986) and Pastor et al. (2002) and it schematises the propagating mass as a one-phase mixture of solid particles and water. The governing equations (3) are solved using the SPH model (Lucy 1977; Gingold and Monaghan 1977).

In SPH model, a given function, $\phi(x)$, and its spatial derivatives can be approximated by integral approximations defined in terms of kernel and they can be further approximated by replacing them with summations over all the corresponding values at the neighbouring particles in a local domain.

234 The following equality is the starting point of SPH approximation:

235 $$\langle \phi(x) \rangle = \int_{\Omega} \phi(x') W(x' - x, h) dx' \quad (7)$$

236 where $\langle \phi(x) \rangle$ is the integral approximation of $\phi(x)$, Ω is the integration domain, $W(x'-x,h)$
237 is the smoothing kernel function and h is the smoothing length defining the influence area
238 of W.

239 The accuracy of the numerical solution and the level of approximation for engineering
240 purposes are a function of the properties and dimensions of the kernel W. In particular, the
241 smoothing kernel function W has to satisfy three main properties: i) its integration returns
242 the unity, ii) when h tends to zero, the kernel function is the Dirac delta function and iii)
243 when |x'-x|>kh, with k a constant that defines the effective area of the smoothing function,
244 W is equal to 0. The latter condition guaranties that the integration over the entire problem
245 domain is localized over the support domain of the smoothing function, which coincides
246 with Ω.

247 Equation 7 is valid at continuum level; since, in problem concerning the propagation of
248 rapid landslide, the information is stored in a discrete framework (e.g. in a series of
249 nodes), the SPH kernel approximation is converted to discretize forms. Thus, the
250 propagating mass is discretized through a set of moving 'particles' or 'nodes' in which
251 regular distributions are used to approximate the values of functions and derivatives. Each
252 node, i, has the following nodal variables: h is the height of of landslide, $\bar{v}$ is the depth
253 averaged velocity, T^b is the surface vector force at the bottom, m is a fictitious mass
254 defined as Ωh, $\bar{p} = \frac{1}{2} b_3 h^2$ is the averaged pressure term and $\overline{\sigma^*}$ is the depth averaged
255 modified stress tensor equals to $\bar{\sigma} + \bar{p}\delta$.

256 As consequence, equation 7 can be rewritten as follow:

257 $$\langle \phi(x_i) \rangle = \sum_{j=1}^{N} \frac{m_j}{\rho_j} \phi(x_j) W_{ij} \quad (8)$$

where ρ_j is the fictitious density of the particle j, N is the number of nodes and W_{ij} is the value of smoothing kernel defined as $W(x_j\text{-}x_i,h)$. Summarizing, the integral approximation of a function $\phi(x)$ at the node i is defined as the sum of the function values estimated at the nodes j, included in the support domain Ω (Figure 2).

Under these hypotheses, the system of equations (3) can be rewritten as:

$$\frac{\bar{d}h_i}{dt} = h_i \sum_j \frac{m_J}{h_J} v_{ij} gradW_{ij} \quad (9)$$

$$\frac{\bar{d}}{dt}\overline{v_i} = -\sum_j m_j \left(\frac{\overline{p_i}}{h_i^2} + \frac{\overline{p_j}}{h_j^2}\right) gradW_{ij} + \frac{1}{\rho}\sum_j m_j \left(\frac{\overline{\sigma_i}^*}{h_i^2} + \frac{\overline{\sigma_j}^*}{h_j^2}\right) gradW_{ij} + b + \frac{1}{\rho h_i}|N^B|T_i^B \quad (10)$$

where v_{ij} is the difference between v_i and v_j and $|N^B| = \left(\frac{\partial Z^2}{\partial x_1} + \frac{\partial Z^2}{\partial x_2} + 1\right)^{\frac{1}{2}}$ with Z the height of the basal surface.

In GeoFlow_SPH code, equations (9) and (10) are discretized in time with the explicit scheme of fourth order Runge Kutta. As in RASH3D, the terrain information are given by DEM; in order to allow searching neighbour particles, an auxiliary temporary structured grid, defined by the minimum smoothing length, covering the part of the terrain covered by SPH particles is used (Figure 2).

The outputs of the code are the values of velocity and depositional height evaluated at each time step.

A detailed description of the method can be found in Pastor et al. (2015).

Figure 2. Nodes and numerical integration on SPH mesh (Pastor et al. 2009, 2014 and 2015).

3.3. Dam break: comparison between numerical and analytical results

This section is devoted to present a benchmark for comparing the predictive capability of the two codes. When numerical models are employed, it is fundamental to know the

accuracy of numerical results by performing analyses on cases that have analytical solutions. This is the case of 1D dam break problem where a vertical wall retaining water suddenly collapses (Figure 3). The propagation domain is assumed dry; that is, there is no water at the right side of the wall before the collapse. Moreover, no internal and basal friction and viscous effects are considered.

Figure 3. 1D dam break problem over a dry bed.

The initial height condition is given by the piecewise constant function:

$$\boldsymbol{h(x,0)} = \begin{cases} \boldsymbol{h_L} & \boldsymbol{if\ x \leq 0} \\ \boldsymbol{0} & \boldsymbol{if\ x > 0} \end{cases} \qquad (11)$$

and the velocity by:

$$u(x,0) = 0 \qquad (12)$$

where h_L is the initial height equals to 10 m.

The analytical solutions (Stoker 1957, Guinot 2003) for 1D dam break problem under the hypothesis of a dry, frictionless bed are:

$$h(x,t) = \begin{cases} h_L & if\ x \leq -2\sqrt{gh_L}t \\ \frac{1}{9g}\left(2\sqrt{gh_L} - \frac{x}{t}\right)^2 & if\ -2\sqrt{gh_L}t \leq x \leq 2\sqrt{gh_L}t \\ 0 & if\ x \geq 2\sqrt{gh_L}t \end{cases} \qquad (11)$$

$$u(x,t) = \begin{cases} 0 & if\ x \leq -\sqrt{gh_L}t \\ \frac{2}{3}\left(\sqrt{gh_L} + \frac{x}{t}\right) & if\ -\sqrt{gh_L}t < x \leq 2\sqrt{gh_L}t \\ 0 & if\ x > 2\sqrt{gh_L}t \end{cases} \qquad (12)$$

Figure 4 shows the comparison between analytical (green dotted line) and numerical results obtained with RASH3D (blue line) and Geoflow_SPH (red line) codes, in terms of flow height (Figure 4a) and velocity (Figure 4b) at t = 0.5 s. A good agreement between analytical and numerical solutions for each code is found. For what it concerns Geoflow_SPH, its computed solution shows a good approximation of the analytical

304 solution especially in the initiation phase of the flow propagation whereas it overestimates
305 flow height (and consequently it underestimates the velocity) during the rarefaction phase.
306 On the contrary, RASH3D solution presents smoother results in the initiation phase (and
307 consequently it there overestimates the velocity) but a good agreement at the flow front.
308
309 **Figure 4.** Comparison between analytical solution and computed results for flow height
310 (a) and velocity (b) at t = 0.5 s.
311
312 **3.4. Frictional dam break on a slope: comparison between numerical and analytical**
313 **results**
314 In the previous section, the prediction capability of the two codes was evaluated solving
315 the 1D problem of the collapse of a vertical wall retaining water and comparing the results
316 with the analytical solution presented by Stoker (1957) and Guinot (2003). Since the two
317 codes are intended for use with granular material, the case of a frictional fluid behind a
318 dam on a slope is here considered (Figure 5). Comparing this benchmark with that
319 presented in section "Dam break: comparison between numerical and analytical results",
320 there are two additional terms, originated by the slope and the basal friction.
321
322 **Figure 5.** The frictional dam break problem on an inclined plane.
323
324 The analytical solution used here to validate the RASH3D and GeoFLow_SPH results was
325 developed by Mangeney et al. 2000 and it allows to easily calculate the flow height and
326 depth-averaged flow velocity for a given time (t) as follow:

327 $$h(t) = \frac{1}{9gcos\theta}\left(2c_0 - \frac{x}{t} + \frac{1}{2}mt\right)^2 \quad (15)$$

328 $$u(t) = \frac{1}{3}\left(2c_0 + \frac{2x}{t} - mt\right) + mt \quad (16)$$

where, g is the gravity acceleration, θ is the slope equals to 30° and the physical quantities c_0 and m are given by the following equations:

$$c_0 = \sqrt{g h_L cos\theta} \quad (17a)$$

$$m = g cos\theta (tan\phi - tan\theta) \quad (17b)$$

where h_L is the initial fluid height and ϕ is the bulk friction angle respectively equal to 10 m and 25°.

The equations (15) and (16) are valid outside the region defined by $x>-c_0t+1/2mt^2$, where the fluid height and the velocity are constant and respectively equal to h_L and mt and upstream from the front of the fluid (h = 0 and u = mt) defined by $x>2c_0t + 1/2mt^2$.

In Figure 6, the comparison between analytical (green dotted line) and numerical results obtained with RASH3D (blue line) and Geoflow_SPH (red line) codes is shown. As in the water dam break case, a good agreement between analytical and numerical solutions for each code was found. For what it concerns flow height, Geoflow_SPH solution presents smoother height values in the initiation phase and a moderate overestimation of the front thickness. RASH3D accentuates the effects of smoothing in the initiation phase but it shows a negligible overestimation of the front thickness values compared to the analytical solution.

About depth-averaged velocity, it has an opposite trend compared to the height flow: in fact, where simulated thickness values are smaller than analytical ones, simulated velocity values are higher and vice-versa. For these reasons, the main differences between numerical and analytical solutions increase closer to the front flow.

Figure 6. Comparison between analytical solution and computed results for flow height (a) and velocity (b) at t = 30 s.

354 The benchmarks here proposed were used to assess the validity of the discretization
355 technique presented. Others validation exercises can be found in Pastor et al. 2009, 2014,
356 2015 and Pirulli 2005.
357
358 ## 4. Case study: the October 2000 Nora Debris flow
359 The Nora stream basin (Figure 7), a tributary of the Orco River (Piedmont region,
360 Northwestern Alps, Italy), was affected in October 2000 by intense rainfall (the average
361 rainfall value was 400 mm in 60 h, with peak rainfall intensity of 28 mm/h) that caused
362 the formation of a debris slide (ARPA Piemonte 2003). Due to the steep drainage network,
363 the intense surface runoff and the altered gneissic bedrock, the debris slide rapidly
364 transformed into a channelized non-cohesive debris flow (Pirulli and Marco 2010).
365 Although residual pockets of debris located along the channel were re-mobilized, due to
366 their smaller volumes then main moving mass, the entrainment of material during runout
367 can be neglected.
368
369 **Figure 7.** Location of the Nora basin (Orco River valley) in Italy.
370
371 Reaching the fan apex, the debris split into two main branches (Figure 8), one on the
372 orographic left with thickness values ranging from 0,5 and 1,5 m; the other, on the
373 orographic right with thickness varying between 0,2 and 0,8 m.
374 After post-event observations (in both the source zone and the depositional areas) and
375 comparison between ground profile pre- and post-event, the bulk debris volume was
376 estimated at approximately 10000 m^3.
377
378 **Figure 8.** Deposition area and debris thickness distribution of the October 2000 Nora
379 debris flow.

5. Discussion

Do different numerical codes that implement the same governing equations (3), but with fundamentally different numerical solvers, give same results or not? Are the differences relevant? What are the consequences concerning the design of potential structural countermeasures?

In order to answer these questions, in the present section the comparison of results coming from analyses performed using the two numerical codes presented above are showed.

The Nora event was already studied and back analysed with the RASH3D code by Pirulli and Marco (2010). The best-fit numerical simulation was obtained using a 5m grid spacing DEM and considering a Voellmy rheology with μ=0,1 and ξ=200 m/s^2.

Note that in contrast with finite difference methods, where pointwise values are approximated, and finite element methods, where basis functions are approximated, in a finite volume method, which is used in RASH3D, the unknowns approximate the average of the solution over the domain grid cell.

Starting from these results, the same analysis, keeping unchanged the rheological parameter values, was carried out using GeoFlow_SPH code. As already mentioned, the meshless particle codes, as GeoFlow_SPH, do not required fixed grid and all of the calculations are performed directly at the particle-centred location. Despite this, beside the 5 m topographic mesh (which provides the topography of the problem), GeoFlow_SPH requires that a secondary grid is used for the debris flow source area definition. In the Rio Nora case, the Authors assumed a 1m spacing secondary grid and consequently a source area made of 212 points was obtained. The smoothing length was set to 2 m.

The topographic mesh resolution for RASH3D code and the secondary grid resolution and dimension of the smoothing length for GeoFlow_SPH have (considering the same computational power) a great weight on the computational time. For the Rio Nora case, the

406 computational time of GeoFlow_SPH code (5m spacing topography grid, 1m spacing
407 secondary grid) is lower than RASH3D one (5m spacing topography grid), since the
408 computations are made on a set of arbitrarily distributed particles (secondary mesh), which
409 are not connected with fixed grid (topography mesh). In particular, using the same
410 workstation, GeoFlow_SPH computation time is less than 20 times with respect to
411 RASH3D.
412 In Figure 9, significant differences can be observed between GeoFlow_SPH and RASH3D
413 simulation especially within the depositional area. In particular:
414 - GeoFlow_SPH overestimates the depositional thickness values with respect to the
415 RASH3D code. It results a zone located at the orographic left of the deposition area
416 where the depositional height reaches 2,7 m (the maximum on site measured
417 depositional height was 1,5 m);
418 - GeoFlow_SPH simulation does not reach a satisfactory approximation of the
419 depositional area shape.
420
421 **Figure 9.** Comparison between RASH (a) and GeoFlow_SPH (b) propagation path
422 (deposition values) at the end of the numerical simulation carried out using Voellmy
423 rheology with μ=0,1 and ξ=200 m/s^2.
424
425 Furthermore, analyzing the flowing path at different time step (Figure 10), it is possible
426 to notice that:
427 - At a given time, the travel distance computed with GeoFlow_SPH is greater than that
428 evaluated with RASH3D code. This means that, being equal the rheological parameter
429 values, the flow simulated in GeoFlow_SPH is faster;
430 - RASH3D simulation evidences a pronounced lateral spreading of the flowing mass.
431

Figure 10. RASH3D (left) and GeoFlow_SPH (right) simulation at different time steps using the same rheological parameters. The two simulations show differences both in term of velocity (flow simulated using SPH is faster) and shape (RASH3D shows a larger lateral spreading).

Figure 11. Comparison of the two numerical code results in terms of velocity differences at time step equal to 50 s (a) and velocity values obtained during whole simulation (b).

Figure 11 shows the differences between velocity values obtained using GeoFlow_SPH and RASH3D at the same time step (a) and the differences between maximum velocity values reached during the whole simulation (b). Analyzing Figure 11a, the above observations are confirmed. It is in fact possible to notice that the positive variation of velocity (dark red color) corresponds to the front of the GeoFlow_SPH simulated flow; on the contrary, the negative variation (dark green) marks the lateral spreading of the RASH3D simulation. Differences between calculated velocities are not appreciable (less than 5 m/s) within the flow body. Concerning the variation of maximum calculated velocities (Figure 11b), it is interesting to underline that the most significant differences are in the upper part of the stream, where the channel is steeper, whereas in correspondence of the alluvial fan there are only appreciable differences between evaluated velocity at the boundary of the deposition area.

Others simulations were run in order to also find the best-fit between depositional area and GeoFlow_SPH results. The best correspondence between depositional height and spatial distribution of the deposit was obtained with μ=0,08 and ξ=100 m/s^2 (Figure 12).

Figure 12. Back calculated GeoFlow_SPH final deposit using Voellmy rheology with μ=0,08 and ξ=100 m/s^2.

458

459 Comparing the numerical results of the two calibrated codes, Figure 13 evidences a good
460 correspondence between the numerically calculated depositional height and in situ
461 surveyed deposit thickness distribution. It is possible, in particular to notice that:

462 - The shape of the flowing mass is slightly different for the two codes: in RASH3D is
463 evident a pronounced lateral spreading along the channel. Furthermore, RASH3D
464 flow shows a greater elongation with respect to GeoFlow_SPH simulated flowing
465 mass.
466 - In this case GeoFlow_SPH velocities are slower than those of RASH3D.

467

468 **Figure 13.** Comparison between RASH3D (left) and GeoFlow_SPH (right) simulation at
469 different time steps using Voellmy rheology with μ=0,1 and ξ=200 m/s^2 and μ=0,08 and
470 ξ=100 m/s^2 respectively.

471

472 **Figure 14.** Differences between maximum velocity values evaluated during the whole
473 simulation using Geoflow_SPH and RASH3D best-fit rheological parameters.

474

475 Analyzing the variation of the maximum velocity values computed using the two codes
476 and their best-fit rheological parameters (Figure 14) it is clear that, along the simulated
477 flow path, there are no relevant differences especially in the depositional area (velocity
478 differences vary between -5 and 5 m/s). The most relevant difference is observed along the
479 boundary of the run out path. RASH3D overestimates the lateral spreading of the flow
480 with respect to GeoFlow_SPH. This aspect also emerges in the most compact
481 configuration of the GeoFlow_SPH deposit with respect to RASH3D.
482 The fact that the rheological parameter values are not interchangeable, from an
483 engineering point of view, has relevant consequences. For instance, hypothesizing the

484 construction of a protection structure at the apex point of the alluvial fan (cfr, Figure 7), it
485 is evident that numerical GeoFlow_SPH velocity is about 10% greater than that calculated
486 using RASH3D best-fit rheological values (Table 1). Instead, there are no differences
487 between the values of maximum flow height.
488
489 **Table 1.** Comparison between numerical results at the apex of alluvial fan calculated
490 using RASH3D and GeoFlow_SPH with the same rheology (Voellmy with μ=0,1 and
491 ξ=200 m/s^2).
492

493 ## 6. Conclusions

494 The two codes RASH3D and GeoFlow_SPH, based on a continuum mechanics approach,
495 were used to back-analyze the debris flow event occurred in October 2000 at the Nora
496 Basin, Northwestern Italian Alps.
497 The presented back analysis evidences that both modelling of past debris flow events and
498 forecasting of future scenarios require to understand and quantify the result discrepancy
499 generated by the use of different numerical codes. The analyses carried out in this paper
500 clearly show that, even if a rheology is selected to back-analyse the same case study with
501 different codes, the obtained calibrated values of rheological parameters are not
502 interchangeable among the codes. This fact has important consequences in the definition
503 of risk scenarios or for planning debris flow countermeasures.
504 Summarizing, the uncertainties related to evaluation of propagation characteristics are
505 consequences of both choice of the numerical code and rheological parameter values. This
506 is a key point that has to be taken into account by practicing engineers that use codes
507 rather than produce them.
508 Concerning the analyzed case, it emerges that:

- Adopting the same rheological parameter values the two codes give different areal depositional distribution and different velocity and thickness values;
- RASH3D code always gives a larger lateral mass spreading with respect to GeoFlow_SPH;
- In order to obtain comparable results in terms of depositional height distribution, the best combination of rheological parameters for GeoFlow_SPH is μ=0,08 and ξ=100 m/s^2;
- The main differences between the two codes are related to velocity values (the GeoFlow_SPH velocity value results 10% greater than the RASH3D ones, by using RASH3D best fit rheological values). No significant differences between maximum depth values are emerged.

References

ARPA Piemonte. 2003. Eventi alluvionali in Piemonte. Evento alluvionale regionale del 13-16 ottobre 2000. Agenzia Regionale per la Protezione Ambientale (ARPA) Piemonte, Turin, Italy.

Audusse, E., Bristeau, M.O., Perthame, B. 2000. Kinetic schemes for Saint-Venant equations with source terms on unstructured grids. Institut National de Recherche en Informatique et Automatique, LeChesnay, France. Rapport de Recherche, No. 3989, 1-44.

Cannon, S.H. 1993. An empirical model for the volume-change behaviour of debris flows. *In* Proceedings of ASCE National Conf. On Hydraulic Engineering, San Francisco, California, July 25-30, 1768-1773.

534 Cascini, L., Cuomo, S., Pastor, M., Sorbino, G. and Piciullo. L. 2014. SPH run-out
535 modelling of channelised landslides of the flow type. Geomorphology ,214, 502–513.
536
537 Corominas, J. 1996. The angle of reach as a mobility index for small and large
538 landslides. Canadian Geotechnical Journal, **33**(2), 260–271.
539
540 Cuomo, S., Pastor, M., Cascini, L., and Castorino. G.C. 2014. Interplay of rheology and
541 entrainment in debris avalanches: a numerical study. Canadian Geotechnical Journal
542 **51**(11): 1318–1330.
543
544 Dutto, P., Stickle, M.M., Pastor, M., Manzanal, D., Yague, A., Tayyebi, and others. 2017.
545 Modelling of Fluidised Geomaterials: The Case of the Aberfan and the Gypsum Tailings
546 Impoundment Flowslides. Materials, **10**, 562, 1-21.
547
548 Gray, J. M. N. T., Wieland, M. and, Hutter, K. 1999. Gravity-driven free surface flow of
549 granular avalanches over complex basal topography. Proc. Royal Soc. London. Ser. A, 455
550 (1841).
551
552 Gingold, R. A., and Monaghan, J. J. 1977. Smoothed particle hydrodynamics: theory and
553 application to non-spherical stars. Monthly Notices of the Royal Astronomical Society,
554 **181**(3), 375–389.
555
556 Guinot, V. 2003. Godunov-type schemes. An introduction for Engineers. Elsevier,
557 Amsterdam.
558

559 Hungr, O. 1995. A model for the runout analysis of rapid flow slides, debris flows, and
560 avalanches. Canadian Geotechnical Journal, **32**(4), 610–623.
561
562 Hungr, O. and Evans, S. G. 1996. Rock avalanche runout prediction using a dynamic
563 model. Landslides, 233–238.
564
565 Hutchinson, J. N. 1986. A sliding–consolidation model for flow slides. Canadian
566 Geotechnical Journal, **23**(2), 115–126.
567
568 Iverson, R. M., and Denlinger, R. P. 2001. "Flow of variably fluidized granular masses
569 across three-dimensional terrain: 1. Coulomb mixture theory." Journal of Geophysical
570 Research: Solid Earth, **106**(B1), 537–552.
571
572 Jakob, M., and Hungr, O. 2005. Debris-flow hazards and related phenomena. Springer-
573 Verlag, Berlin.
574
575 Lucy, L. B. 1977. A numerical approach to the testing of the fission hypothesis. The
576 Astronomical Journal, **82**, 1013.
577
578 Mangeney, A., Heinrich, P., Roche, R. 2000. Analytical Solution for Testing Debris
579 Avalanche Numerical Models. Pure appl. geophys. **157**, 1081–1096.
580
581 Mangeney-Castelnau A., Vilotte J.-P., Bristeau M.O., Perthame B., Bouchut F., Simeoni
582 C., Yernini S. 2003. Numerical modelling of avalanches based on Saint-Venant equations
583 using a kinetic scheme. Journal Geophys. Res. **108** (B11), 1-18.
584

585 Manzella, I., Pirulli, M., Naaim, M., Serratrice, J.F., Labiouse, V. 2008. Numerical
586 modelling of a rock avalanche laboratory experiment in the framework of the
587 “Rockslidetec” alpine project. *In* Landslides and Engineered Slopes: Procs. 10th
588 International Symposium on Landslides and Engineered Slopes. *Edited by* Chen Z. et al.;
589 Xi’an, Cina, 30 Giugno - 4 Luglio 2008, Taylor & Francis Group, London, Vol. 1, 835-
590 841.
591
592 Mcdougall, S., and Hungr, O. 2005. Dynamic modelling of entrainment in rapid
593 landslides. Canadian Geotechnical Journal, **42**(5), 1437–1448.
594
595 O'brien, J. S., Julien, P. Y., and Fullerton, W. T. 1993. Two-Dimensional Water Flood and
596 Mudflow Simulation. Journal of Hydraulic Engineering, **119**(2), 244–261.
597
598 Pastor, M., Quecedo, M., Merodo, J. A. F., Herrores, M. I., González, E., and Mira, P.
599 2002. Modelling tailings dams and mine waste dumps failures. Géotechnique, **52**(8), 579–
600 591.
601
602 Pastor, M., Blanc, T., Pastor, M.J., Sanchez, M., Haddad, B., Mira, P., Fernandez Merodo,
603 J.A., Herreros, I., and Drempetic, V. 2007. A SPH depth integrated model with pore
604 pressure coupling for fast landslides and related phenomena. *In* Procs. of the 2007
605 International Forum on Landslide Disaster Management, *Edited by* K. Ho and V. Li, Hong
606 Kong, 10-12 December 2007, Vol. II, 987-1014.
607
608 Pastor, M., Haddad, B., Sorbino, G., Cuomo, S., and Drempetic, V. 2009. A depth-
609 integrated, coupled SPH model for flow-like landslides and related

610 phenomena. International Journal for Numerical and Analytical Methods in Geomechanics,
611 **33**(2), 143–172.
612
613 Pastor, M., Haddad, V., Mira, P., Fernandez-Merodo, J.A. 2014. Depth averaged models
614 for rock avalanche propagation: an SPH approach. *In* Rock Slope Stability 2014;
615 Marrakesh, Morocco, 2 - 4 April 2014, 35-58.
616
617 Pastor, M., T. Blanc, B. Haddad, V. Drempetic, Mila Sanchez Morles, P. Dutto, and
618 others. 2015. Depth Averaged Models for Fast Landslide Propagation: Mathematical,
619 Rheological and Numerical Aspects. Archives of Computational Methods in Engineering.
620 **22**, 67–104.
621
622 Pirulli, M. 2005. Numerical modelling of landslide runout, a continuum mechanics
623 approach. Ph.D dissertation, Politecnico of Turin, Turin, Italy.
624
625 Pirulli, M., Scavia, C. 2007. A set of benchmark tests to assess the performance of a
626 continuum mechanics depth-integrated model. *In* Procs. of the 2007 International Forum
627 on Landslide Disaster Management, *Edited by* K. Ho and V. Li, Hong Kong, 10-12
628 December 2007, Vol. II, 1015-1042.
629
630 Pirulli, M., and Sorbino, G. 2008. Assessing potential debris flow runout: a comparison of
631 two simulation models. Natural Hazards and Earth System Science, **8**(4), 961–971.
632
633 Pirulli, M. 2009. The Thurwieser rock avalanche (Italian Alps): Description and dynamic
634 analysis. Engineering Geology, **109**(1-2), 80–92.
635

636 Pirulli, M., and Marco, F. 2010. Description and numerical modelling of the October 2000
637 Nora debris flow, Northwestern Italian Alps. Canadian Geotechnical Journal, **47**(2), 135–
638 146.
639
640 Pirulli, M., and Pastor, M. 2012. Numerical study on the entrainment of bed material into
641 rapid landslides. Geotechnique, **62**(11), 959-972.
642
643 Pirulli, M. 2016. Numerical simulation of possible evolution scenarios of the Rosone
644 deep-seated gravitational slope deformation (Italian Alps, Piedmont). Rock Mechanics and
645 Rock Engineering, **49**(6), 2373-2388.
646
647 Pirulli, M., Barbero, M., Marchelli, M., and Scavia, C. 2017. The failure of the Stava
648 Valley tailings dams (Northern Italy): numerical analysis of the flow dynamics and
649 rheological properties. Geoenvironmental Disasters, **4**(3), 1-15.
650
651 Pisani, G., Pirulli, M., Labiouse, V., and Scavia, C. 2013. Influence of bed curvature on
652 the numerical modelling of unconstrained granular materials. *In* Landslide Science and
653 Practice - Volume 3: Spatial Analysis and Modelling; *Edited by* Margottini, C., Canuti, P.,
654 and Sassa, K.; Springer - Berlin; pp. 271-276.
655
656 Pouliquen, O. 1999. Scaling laws in granular flows down rough inclined planes. Physics of
657 fluids, **11**(3), 542-548.
658
659 Revellino, P., Hungr, O., Guadagno, F. M., and Evans, S. G. 2004. Velocity and runout
660 simulation of destructive debris flows and debris avalanches in pyroclastic deposits,
661 Campania region, Italy. Environmental Geology, **45**(3), 295–311.

662

663 Rickenmann, D., and Koch, T. 1997. Comparison of debris flow modelling approaches. *In*
664 Proceedings of the 1st Int. Conf. On Debris Flow Hazards Mitigation: Mechanics,
665 Prediction and Assessment, ASCE, Reston, VA, USA, 576-585.

666

667 Rickenmann, D. 1999. Empirical relationships for debris flows. Natural Hazards, **19**(1),
668 47–77.

669

670 Rickenmann, D. 2005. Runout prediction methods. Debris-flow Hazards and Related
671 Phenomena Springer Praxis Books, 305–324.

672

673 Sauthier, C., Pirulli, M., Pisani, G., Scavia, C., Labiouse, V. (2015). Numerical modelling
674 of gravel unconstrained flow experiments with the DAN3D and RASH3D codes.
675 Computers & Geosciences, **85**, 81-90.

676

677 Savage, S. B., and Hutter, K. 1989. The motion of a finite mass of granular material down
678 a rough incline. Journal of Fluid Mechanics, **199**(1), 177.

679

680 Stoker, JJ. 1953. Water Waves. Interscience: New York.

681

682 Vagnon, F. 2017. Theoretical and experimental study on the barrier optimization against
683 debris flow risk. Ph.D dissertation, University of Turin, Turin, Italy.

684

List of symbols

B(U) = source term;

DEM = Digital Elevation Model;

$\Phi(x)$ = given function;

$\langle\Phi(x)\rangle$ = integral approximation of the given function;

F(U) = flux term;

g = gravitational acceleration;

H = characteristic flow thickness;

L = characteristic length of flowing mass;

m_i = node mass;

n_b = unit vector normal to bed;

N = number of nodes;

μ = frictional coefficient;

ξ = turbolent coefficient;

$\overline{p_i}$ = average pressure term;

ρ = mass density;

Ω = integration domain;

SPH = Smooth Particle Hydrodynamics.

$\sigma(x,y,z,t)$ = Cauchy stress tensor;

$T(T_x, T_y, T_z)$ = traction vector;

t_{ib} = surface vector force at the bottom of the flow;

τ = shear stress;

$v = (v_x, v_y, v_z)$ = flow velocity;

$\bar{v} = \left(\overline{v_x}, \overline{v_y}\right)$ = depth-averaged flow velocity;

U = velocity vector;

W = kernel of linear function.

Tables

Table 1. Comparison between numerical results at the apex of alluvial fan calculated using RASH3D and GeoFlow_SPH with the same rheology (Voellmy with μ=0,1 and ξ=200 m/s^2).

Code	Rheological law	v_{max} [m/s]	h_{max} [m]
RASH3D	Voellmy: μ=0.1 - ξ=200 m/s^2	8,76	2,04
GeoFlow_SPH		9,57	2,05

Figure captions

Figure 1. Triangular finite-element mesh for dual cell C_i (adapted from Mangeney-Castelnau et al. 2003). n_{ij} normal vector to Γ_{ij} directed from P_i to P_j, one of the mesh vertexes that surround P_i, Γ_{ij}, boundary of the dual cell C_i separating P_i from P_j.

Figure 2. Nodes and numerical integration on SPH mesh (Pastor et al. 2009)

Figure 3. 1D dam break problem over a dry bed.

Figure 4. Comparison between analytical solution and computed results for flow height (a) and velocity (b) at t = 0.5 s.

Figure 5. The frictional dam break problem on an inclined plane.

Figure 6. Comparison between analytical solution and computed results for flow height (a) and velocity (b) at t = 30 s.

Figure 7. Location of the Nora basin (Orco River valley) in Italy.

Figure 8. Deposition area and debris thickness distribution of the October 2000 Nora debris flow.

Figure 9. Comparison between RASH (a) and GeoFlow_SPH (b) propagation path (deposition values) at the end of the numerical simulation carried out using Voellmy rheology with μ=0,1 and ξ=200 m/s^2.

Figure 10. RASH3D (left) and GeoFlow_SPH (right) simulation at different time steps using the same rheological parameters. The two simulations show differences both in term of velocity (flow simulated using SPH is faster) and shape (RASH3D shows a larger lateral spreading).

Figure 11. Comparison of the two numerical code results in terms of velocity differences at time step equal to 50 s (a) and velocity values obtained during whole simulation (b).

Figure 12. Back calculated GeoFlow_SPH final deposit using Voellmy rheology with μ=0,08 and ξ=100 m/s^2.

742 **Figure 13.** Comparison between RASH3D (left) and GeoFlow_SPH (right) simulation at
743 different time steps using Voellmy rheology with μ=0,1 and ξ=200 m/s^2 and μ=0,08 and
744 ξ=100 m/s^2 respectively.
745 **Figure 14.** Differences between maximum velocity values evaluated during the whole
746 simulation using Geoflow_SPH and RASH3D best-fit rheological parameters.
747

748

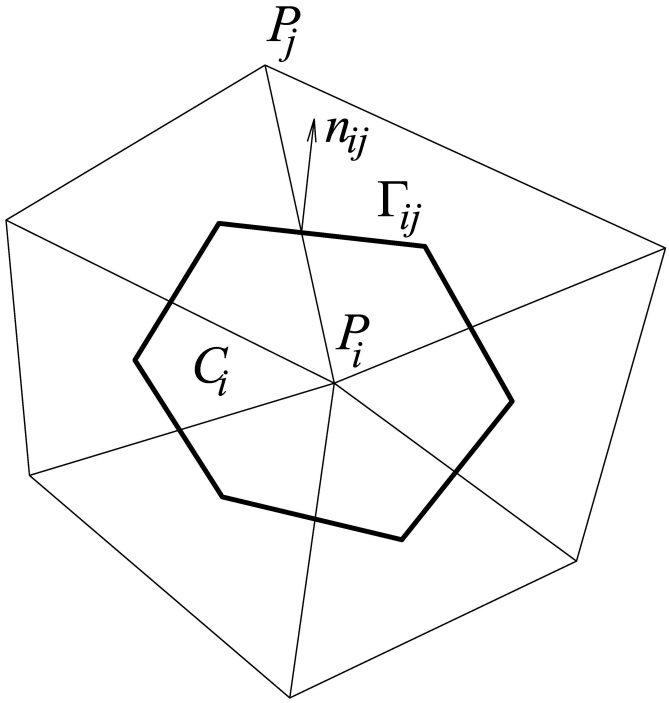

749

750 **Figure 1.** Triangular finite-element mesh for dual cell C_i (adapted from Mangeney-
751 Castelnau et al. 2003). n_{ij} normal vector to Γ_{ij} directed from P_i to P_j, one of the mesh
752 vertexes that surround P_i, Γ_{ij}, boundary of the dual cell C_i separating P_i from P_j.

753

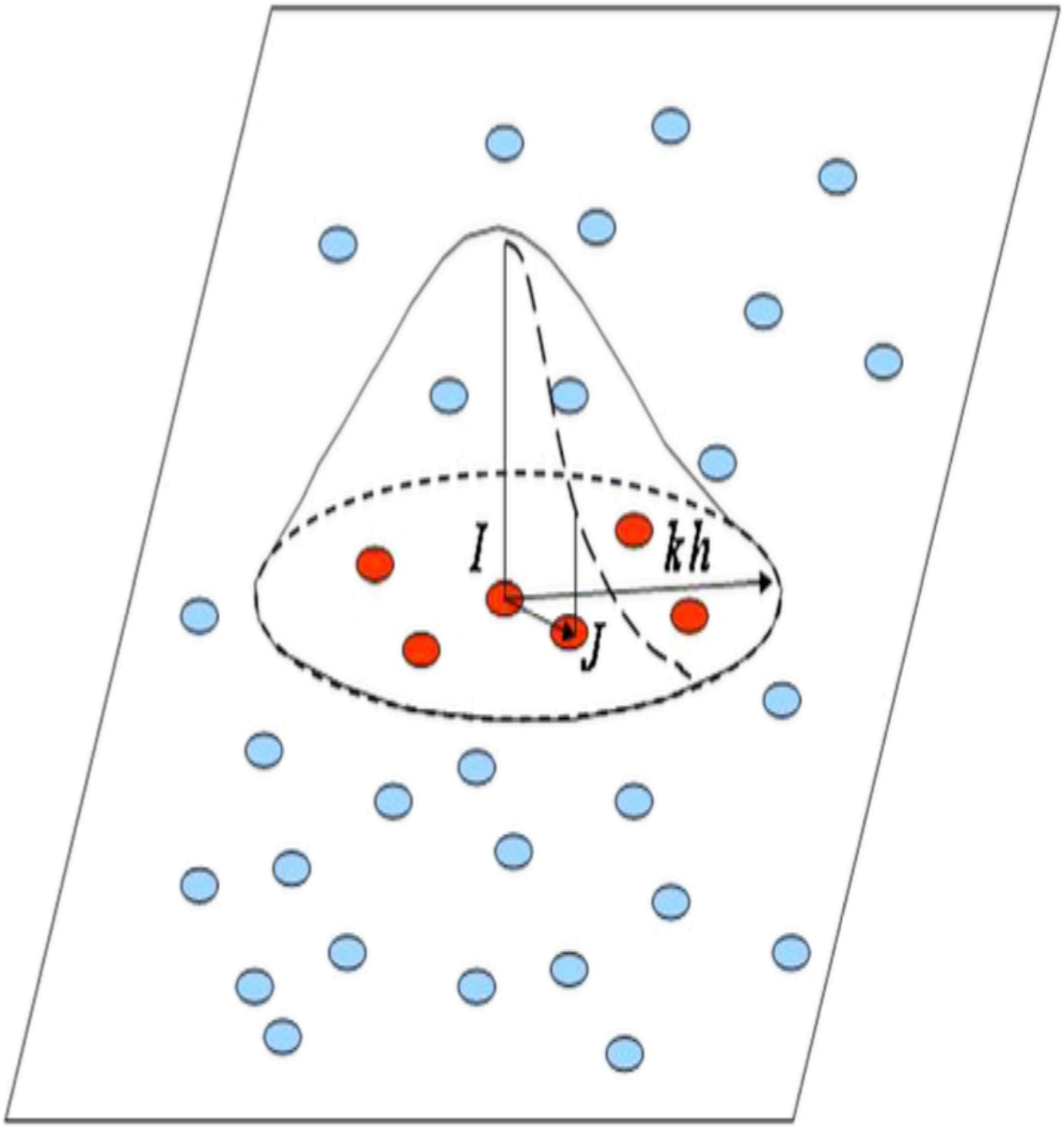

754

755 **Figure 2.** Nodes and numerical integration on SPH mesh (Pastor et al. 2009)

756

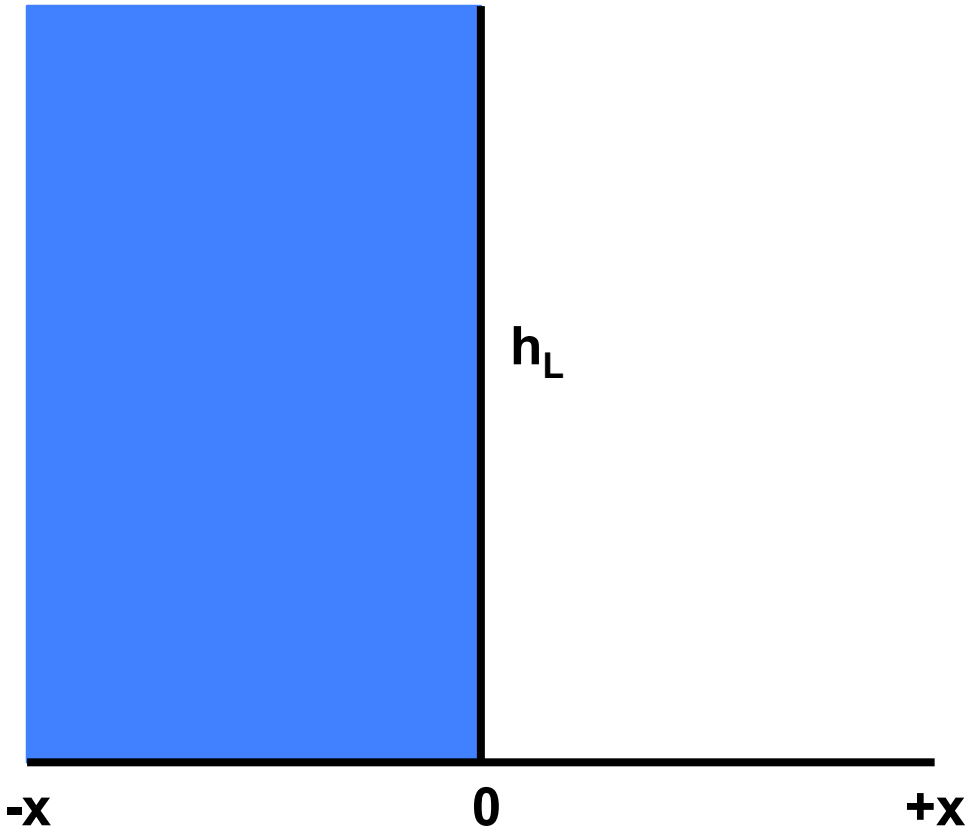

757

758 **Figure 3.** 1D dam break problem over a dry bed.

759

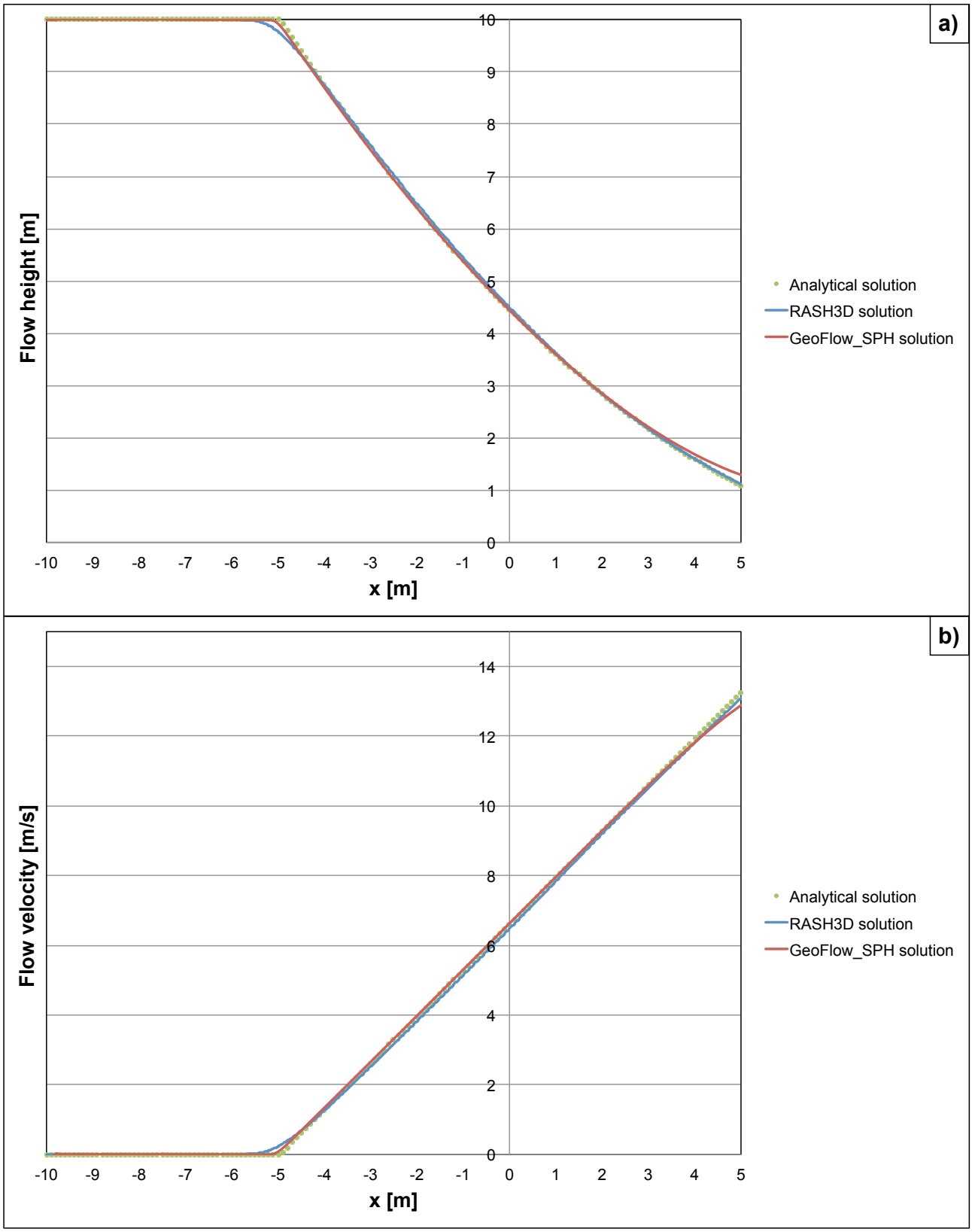

760

761 **Figure 4.** Comparison between analytical solution and computed results for flow height

762 (a) and velocity (b) at t = 0.5 s.

763

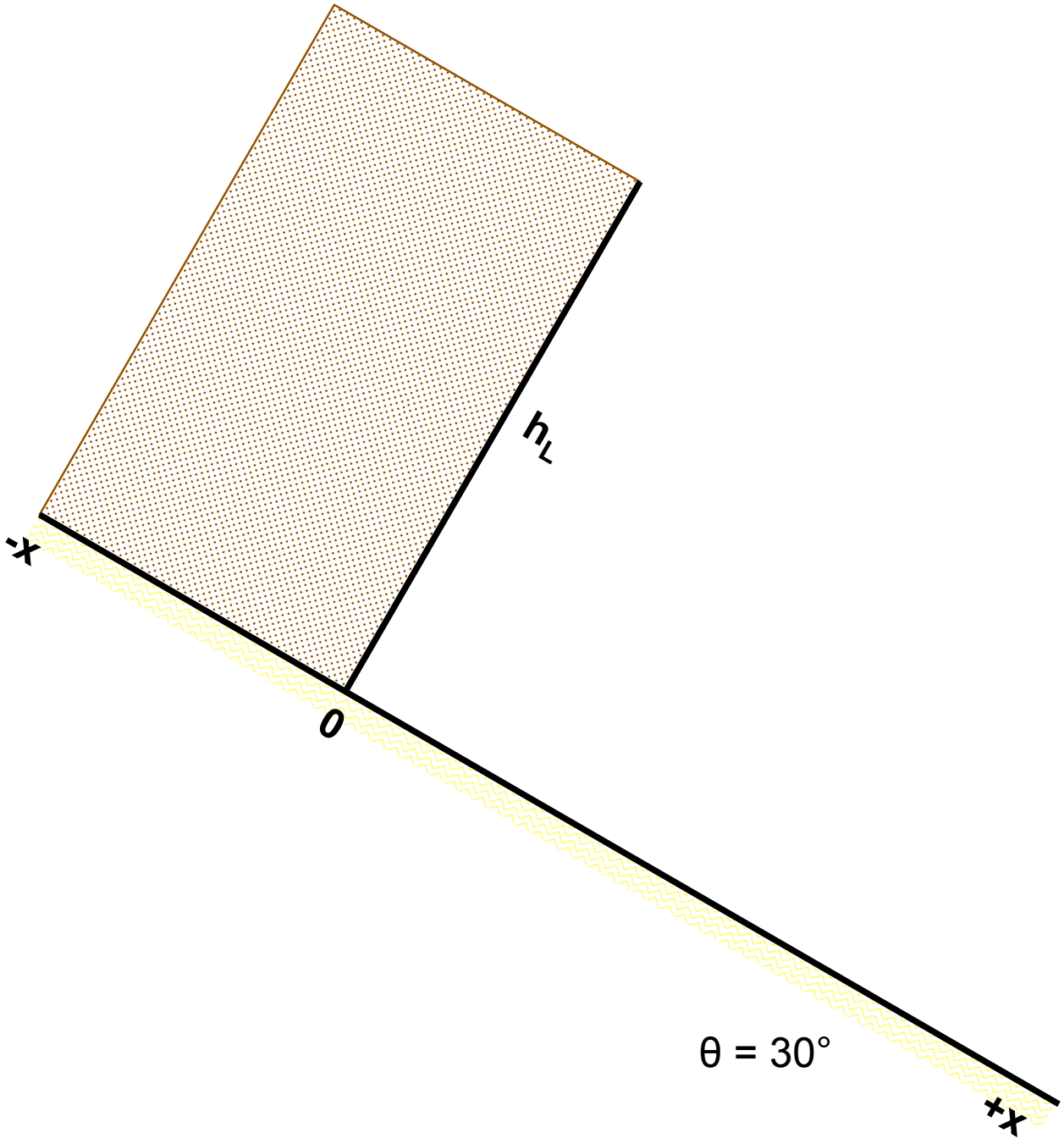

764

765 **Figure 5.** The frictional dam break problem on an inclined plane.

766

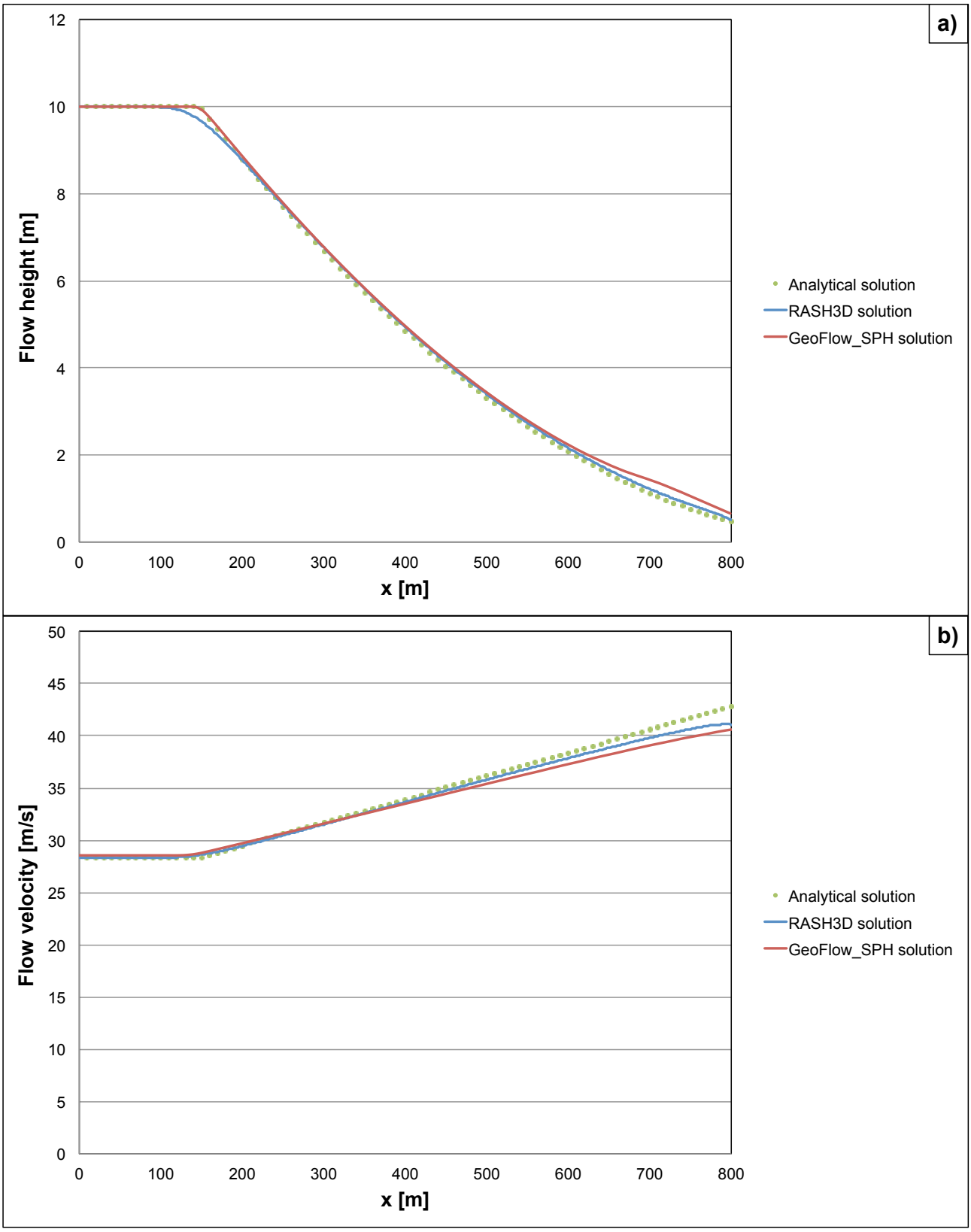

767

768 **Figure 6.** Comparison between analytical solution and computed results for flow height

769 (a) and velocity (b) at t = 30 s.

770

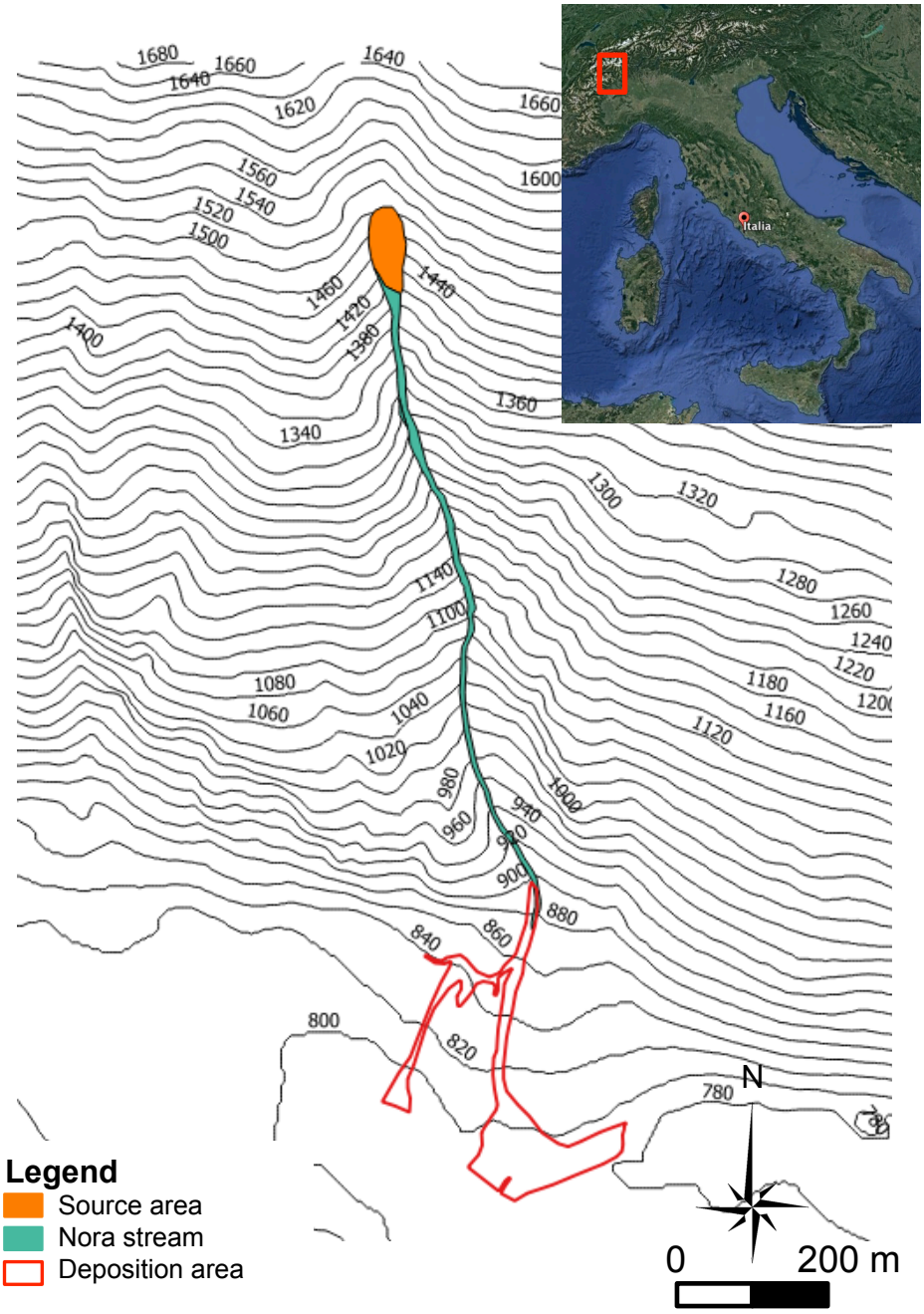

771

772 **Figure 7.** Location of the Nora basin (Orco River valley) in Italy.

773

774

775 **Figure 8.** Deposition area and debris thickness distribution of the October 2000 Nora

776 debris flow.

777

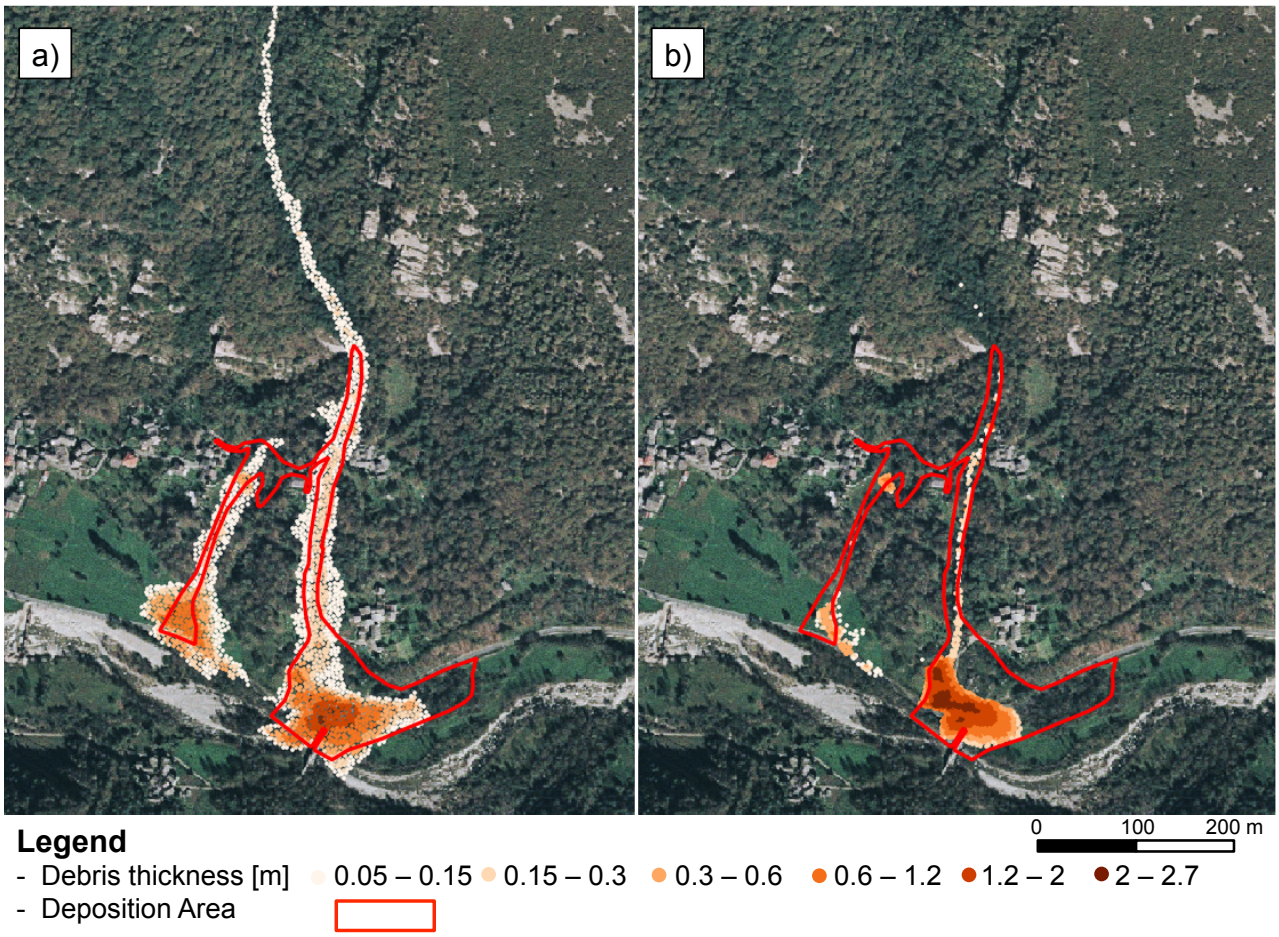

778

779 **Figure 9.** Comparison between RASH (a) and GeoFlow_SPH (b) propagation path
780 (deposition values) at the end of the numerical simulation carried out using Voellmy
781 rheology with μ=0,1 and ξ=200 m/s^2.

782

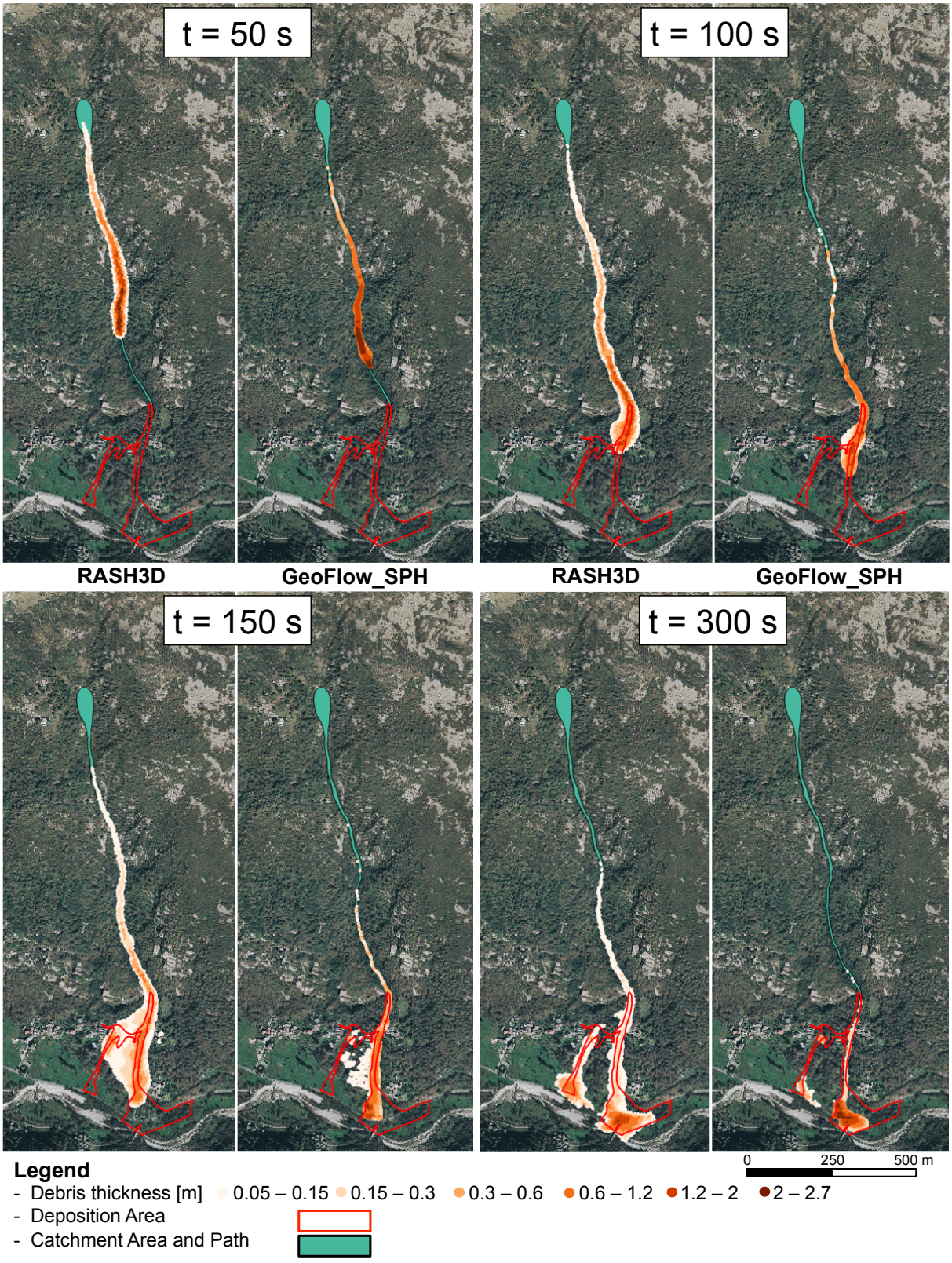

783

784 **Figure 10.** RASH3D (left) and GeoFlow_SPH (right) simulation at different time steps
785 using the same rheological parameters. The two simulations show differences both in term
786 of velocity (flow simulated using SPH is faster) and shape (RASH3D shows a larger
787 lateral spreading).

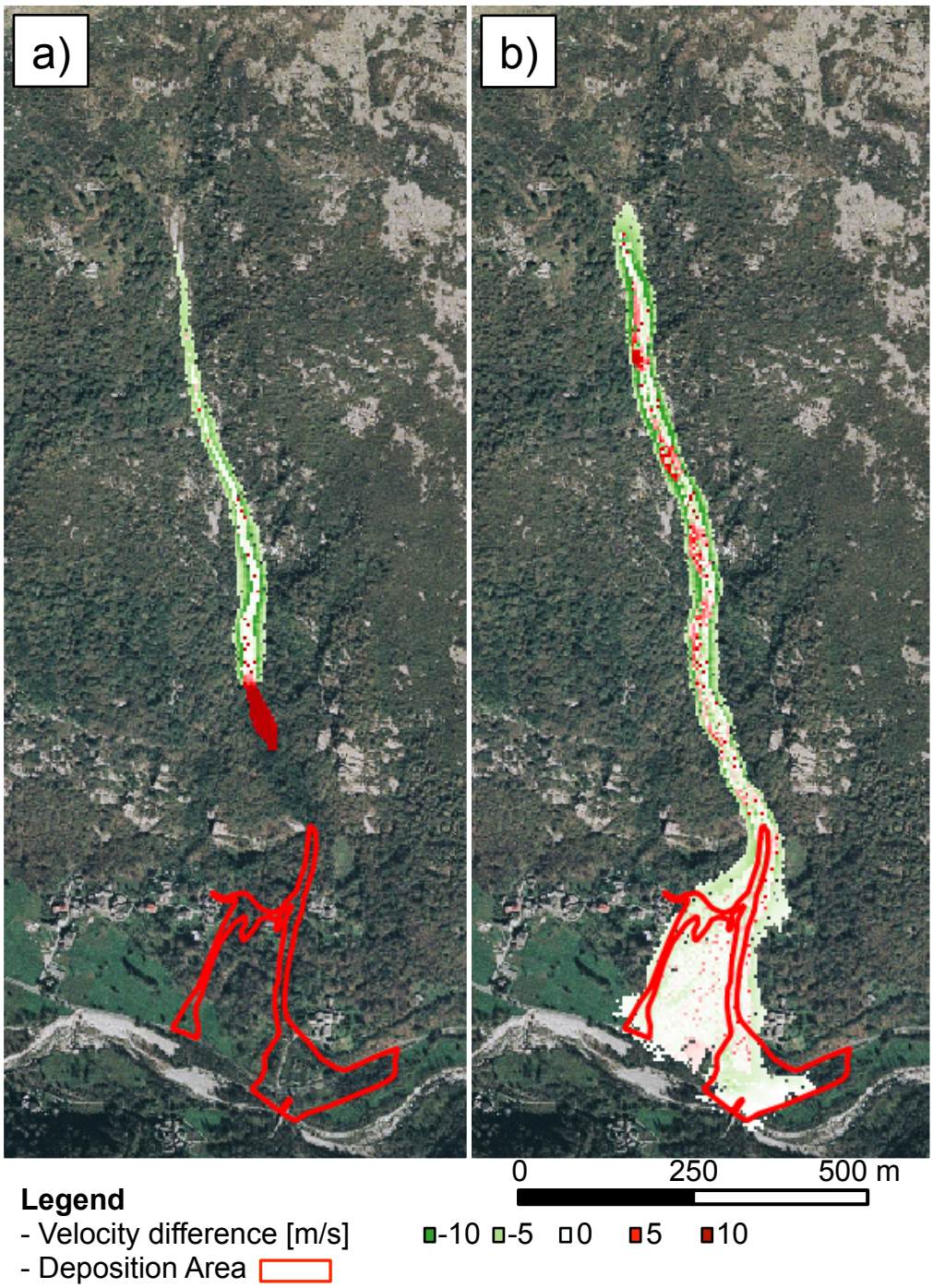

788

789 **Figure 11.** Comparison of the two numerical code results in terms of velocity differences

790 at time step equal to 50 s (a) and velocity values obtained during whole simulation (b).

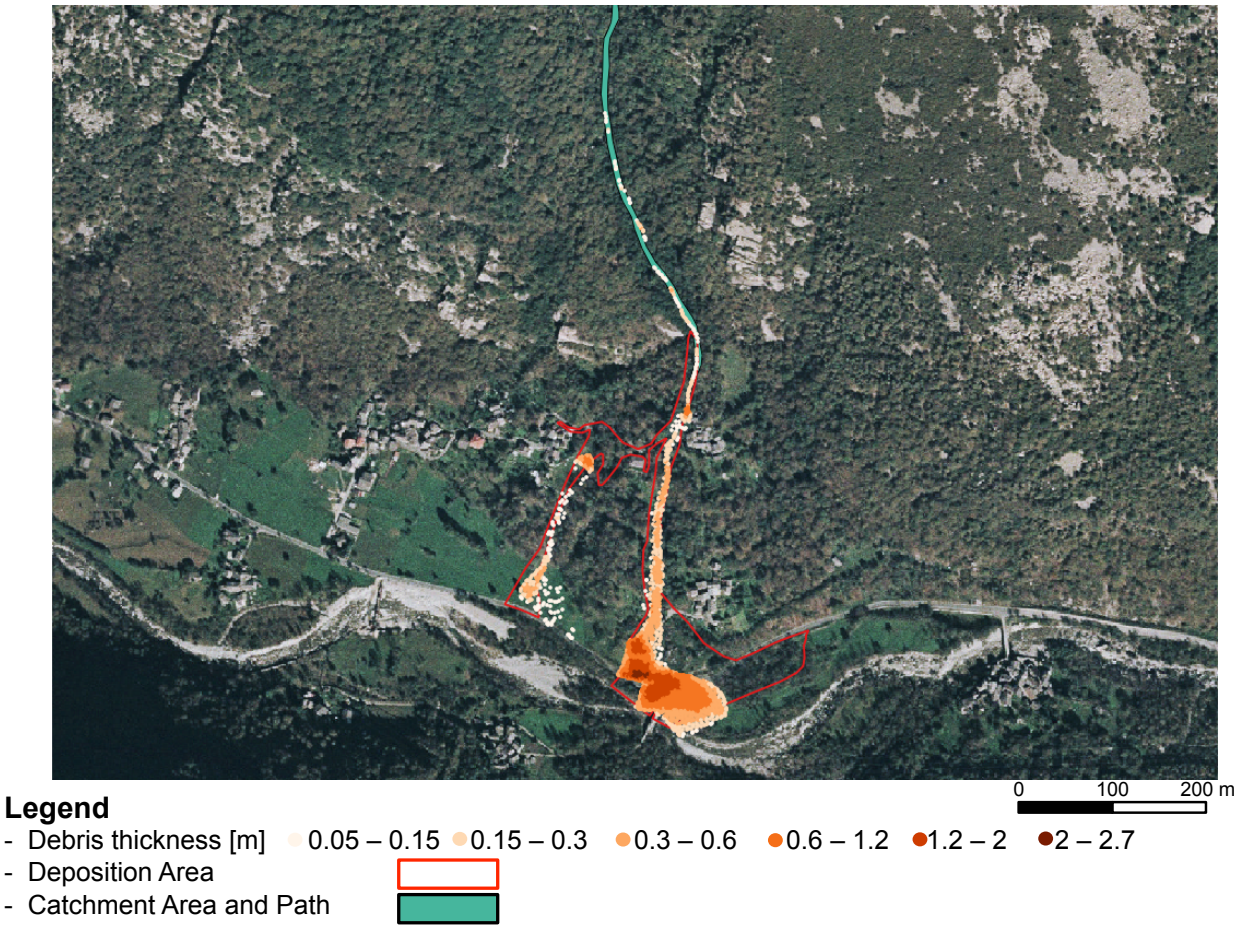

791

792 **Figure 12.** Back calculated GeoFlow_SPH final deposit using Voellmy rheology with

793 μ=0,08 and ξ=100 m/s^2.

794

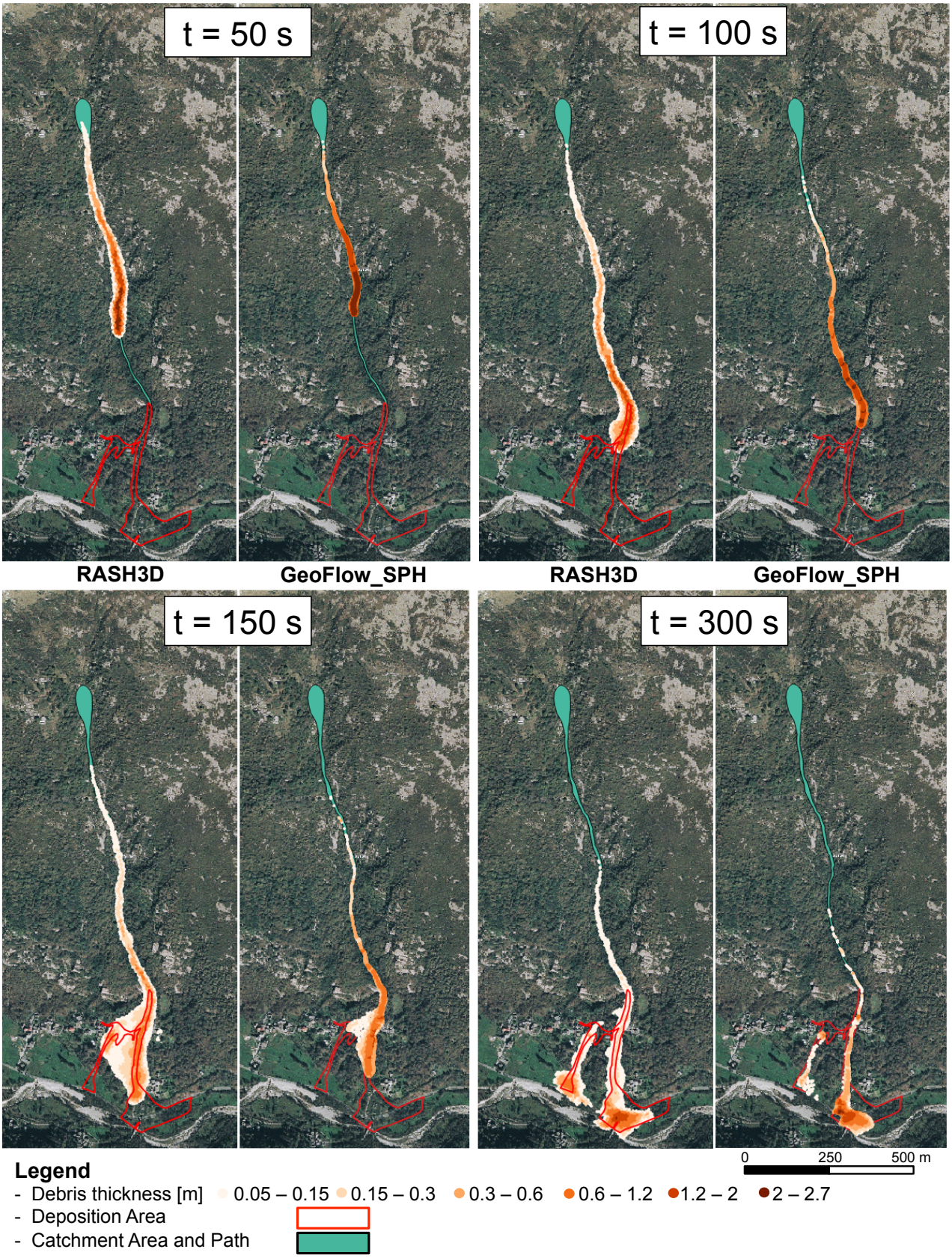

795

796 **Figure 13.** Comparison between RASH3D (left) and GeoFlow_SPH (right) simulation at
797 different time steps using Voellmy rheology with μ=0,1 and ξ=200 m/s^2 and μ=0,08 and
798 ξ=100 m/s^2 respectively.

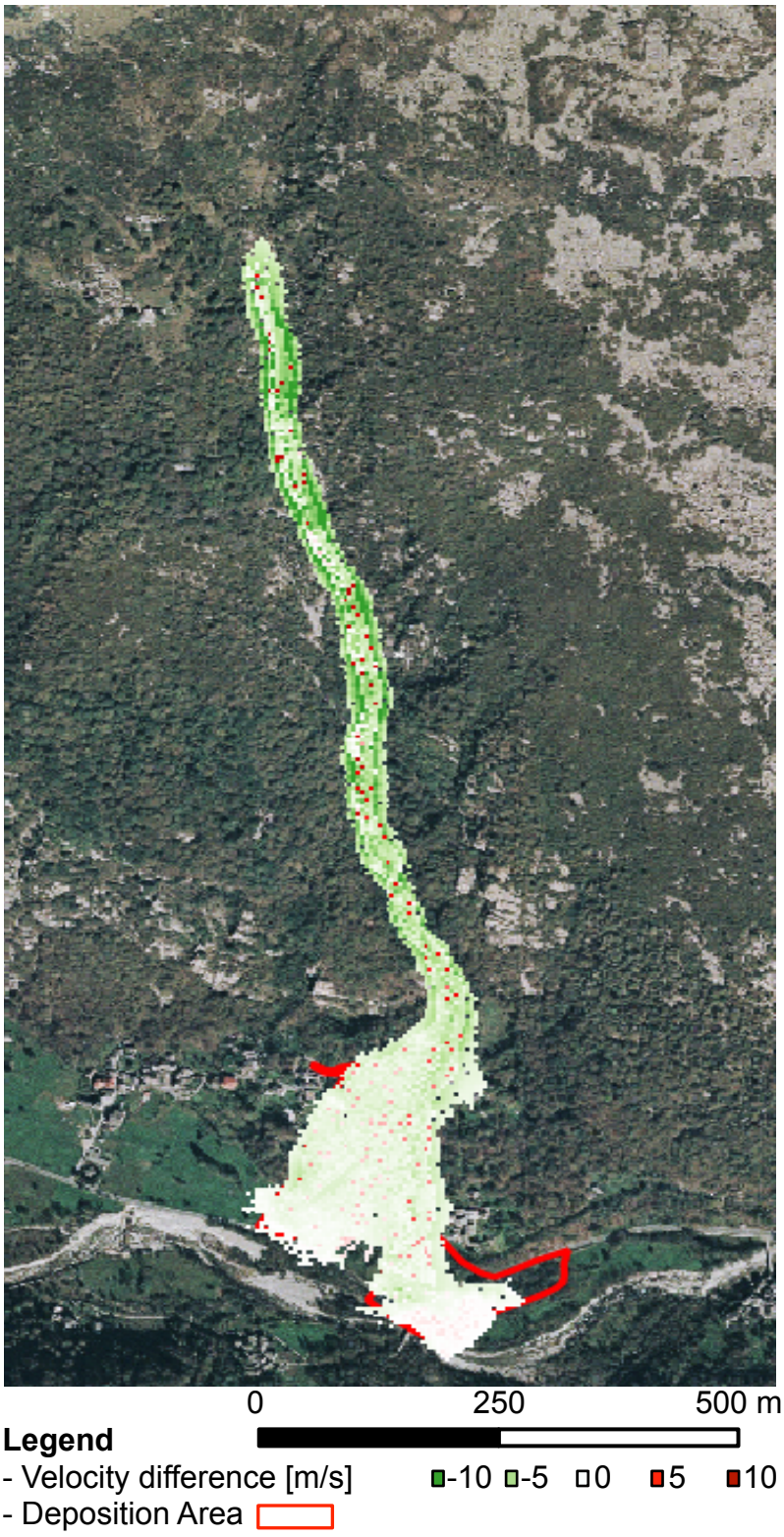

799

800 **Figure 14.** Differences between maximum velocity values evaluated during the whole

801 simulation using Geoflow_SPH and RASH3D best-fit rheological parameters.

802